How will radar layover impact SWOT measurements of water surface elevation and slope, and estimates of river discharge?

Michael Durand[a,*], Curtis Chen[b], Renato Prata de Moraes Frasson[a,b], Tamlin M. Pavelsky[c], Brent Williams[b], Xiao Yang[c], Alex Fore[b]

[a] The Ohio State University, School of Earth Sciences and Byrd Polar and Climate Research Center, Columbus 43214, USA
[b] NASA Jet Propulsion Laboratory, California Institute of Technology, Pasadena 91109, USA
[c] Department of Geological Sciences, University of North Carolina, Chapel Hill 27599-3315, USA

ARTICLE INFO

Keywords:
River hydrology
Radar interferometry

ABSTRACT

Water surface elevation (WSE), slope and width measurements from the forthcoming Surface Water and Ocean Topography (SWOT) mission will enable spaceborne estimates of global river discharge. WSE will be measured by interferometric synthetic aperture radar (InSAR). InSAR measurements are vulnerable to contamination from layover, a phenomenon wherein radar returns from multiple locations arrive at the sensor simultaneously, rendering them indistinguishable. This study assesses whether layover will significantly impact the precision of SWOT estimates of global river discharge. We present a theoretical river layover uncertainty model at the scale of nodes and reaches, which constitute nominal 200 m and 10 km averages, respectively, along river centerlines. The model is calibrated using high-resolution simulations of SWOT radar interaction with topography covering a total of 41,233 node observations, across a wide range of near-river topographic features. We find that height uncertainty increases to a maximum value at relatively low values of topographic standard deviation and varies strongly with position in the swath. When applied at global scale, the calibrated model shows that layover causes expected height uncertainty to increase by only a modest amount (from 9.4 to 10.4 cm at the 68th percentile). The 68th percentile of the slope uncertainty increases more significantly, from 10 to 17 mm/km. Nonetheless, the 68th percentile discharge uncertainty increases only marginally. We find that the impact of layover on SWOT river discharge is expected to be small in most environments.

1. Introduction

The forthcoming Surface Water and Ocean Topography (SWOT) satellite mission will provide new observations of global river processes (Pavelsky et al., 2014), and of global lakes and oceans. The Ka-band Radar Interferometer (KaRIn) instrument (Fjørtoft et al., 2014) aboard SWOT will measure radar returns at near-nadir incidence angles (0.7–4.3°). Gridded radar imagery produced by KaRIn will be geolocated, mapped onto river centerlines, and used to measure river height, width and slope (Frasson et al., 2017). River data products will be produced for rivers greater than 100 m in width, and perhaps as narrow as 50 m (Esteban Fernandez, 2017). SWOT height, width and slope measurements will be combined with flow resistance laws to estimate river discharge (Biancamaria et al., 2016).

One potential source of error that is expected to affect SWOT measurements is the so-called "layover" phenomenon; layover occurs when radar returns from multiple spatial locations arrive at the sensor simultaneously. For any radar system, layover will occur whenever terrain slope is greater than the radar incidence angle. Thus, layover problems tend to be most prevalent in areas of high topographic variability (Rees, 2001; Bamler and Hartl, 1998), if one assumes spatially uniform radar reflectivity across the scene.

While layover is thus expected to be ubiquitous at SWOT near-nadir incidence angles, as illustrated graphically in Fig. 1, the effect of the differing land and water radar reflectivities largely mitigates layover impacts on SWOT measurements of water (Fjørtoft et al., 2014), as will be shown in this paper. KaRIn radar waves incident on water surfaces are likely to reflect back toward the KaRIn sensor, whereas radar waves incident on land surfaces are more likely to scatter away from the KaRIn sensor. Thus, for SWOT, water is generally far "brighter" than land. As a result, layover from land near rivers is not expected to completely obscure SWOT measurements of rivers, but rather to affect the precision of SWOT measurements of river height and slope (Frasson et al., 2017), thereby also affecting river discharge estimates. Layover effects on

* Corresponding author.
E-mail address: durand.8@osu.edu (M. Durand).

https://doi.org/10.1016/j.rse.2020.111883
Received 13 November 2019; Received in revised form 7 May 2020; Accepted 9 May 2020
Available online 01 July 2020

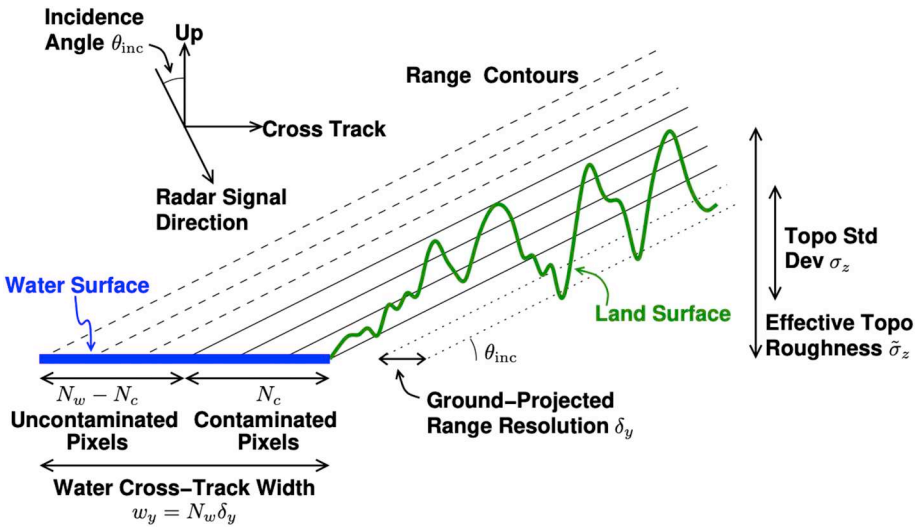

Fig. 1. Illustration of the relationship between the topographic roughness and the extent of layover contamination. In this graphic, scales and angles are exaggerated greatly for illustration. The solid black range-resolution contours are those that intersect both the desired water surface and the undesired land surface, while the dashed black range contours are those that intersect only the water surface, and the dotted black range contours are those that intersect only the land surface. Note that the vertical arrows on the right side of the illustration do not necessarily correspond to the actual standard deviation of the land surface as drawn. These are shown merely for illustrative purposes.

discharge have not previously been quantified, however.

In this paper we quantify the global impacts of layover on river height, slope and discharge estimates. Specifically, we formulate a theoretical model that predicts layover impact on river height and slope uncertainty as a function of surface topography standard deviation (see Fig. 1). We calibrate and validate the model on a set of first-principles simulations of SWOT radar measurements of rivers and the surrounding landscapes derived from high-resolution land cover and topographic data. We then estimate accuracy and precision of global SWOT river height and slope measurements by applying the layover model to a global river database. We use first-order error propagation to compute the uncertainty in river discharge as a function of the precision of SWOT observations, and thereby provide a discussion of the expected impacts of layover on SWOT river science.

2. Data

2.1. United States geologic survey Lidar point clouds

True surface topography datasets used in the first-principles radar simulations are 3D elevation program (3DEP) Lidar Point Clouds (LPCs) similar to those described by USGS (2017), but obtained from the USGS Earth Resources Observations and Science Center in 2014 via personal communication (note that the radar simulations themselves are described in Section 3.2). A total of 40 LPC Digital Elevation Models (DEMs) are used for this study, all from the coterminous United States (CONUS); LPC domains are shown in Fig. 2. While LPCs are also available from areas outside CONUS, we chose to use only the 3DEP dataset as it is self-consistent, and representative of global river statistics, as shown in Section 3.2. The LPC domains vary in size from 6000 to 16,500 km^2. A majority of the LPCs are in fairly flat areas in the Eastern United States (Fig. 2a), although there is one LPC from Western United States, and several with higher topographic relief (e.g. Fig. 2b and Fig. 2c). The domain median topographic roughness (defined in Section 3.1) for river nodes varies widely from 2.8 m to 56.5 m; the LPC domains shown in Fig. 2b and Fig. 2c have topographic roughnesses of 19.8 m and 56.5 m, respectively. The LPCs include a wide variety of river size and geomorphology: median river widths within LPC domains range from 46.7 m to 849.1 m. The spatial posting of typical LPCs varies but is typically less than one meter. The 3DEP data often include both first return (representing vegetation canopy) and ground elevation.

2.2. Shuttle radar topography mission digital elevation model

SWOT processing requires a so-called “reference” DEM to process the radar returns. The 30 m Shuttle Radar Topography (SRTM) mission (Farr et al., 2007) DEM version 3 (NASA JPL, 2013b) is used as the reference DEM for processing the first-principles radar simulations as described in Section 3.2. Additionally, the 3 arcsec SRTM DEM version 4 (Jarvis et al., 2008) is used to compute the topographic roughness (defined in Section 3.1), one of the inputs to the parameterized layover model, which is independent of the SWOT processing that uses the higher-resolution DEM. The lower-resolution DEM facilitates the global-scale analysis because of its lower data volume; it is appropriate for computing the topographic roughness because this quantity is dominated by large-scale features (this is confirmed by our analysis but not shown in this paper).

2.3. Global river database

As part of SWOT processing, and as part of the radar simulations described in Section 3.1, two-dimensional SWOT radar pixels are mapped onto river centerlines, as described in Section 3.2. The centerlines themselves are contained in a River Database derived from the Global River Width from Landsat (GRWL) database produced by Allen and Pavelsky (2018). The River Database delineates river centerlines using point features located every 30 to 42.4 m. The database contains pre-specified locations of river nodes (point features spaced approximately every 200 m along the river) and river reaches (nominally 10 km in length). Database width, water surface slope, and river discharge are identical to those from Frasson et al. (2019), and are used in the propagation of layover induced errors to SWOT discharge estimates, as described in Section 3.4.

2.4. Additional datasets

The true water mask for the radar simulations was derived from a combination of the National Hydrography Dataset (USGS, 2019), the SRTM Water Body Dataset (NASA JPL, 2013a) and the global river database described previously. Land types from the 2011 National Land

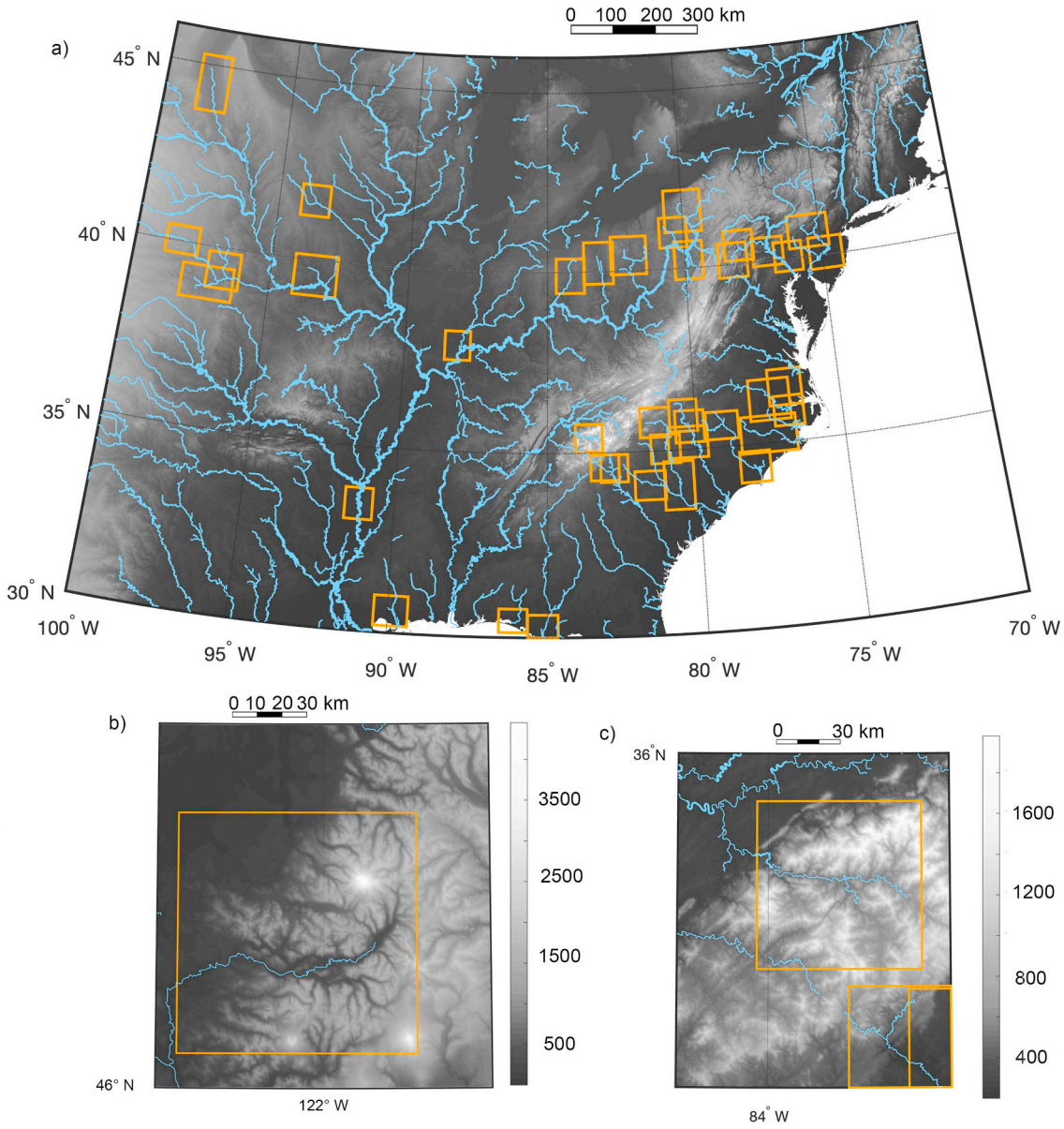

Fig. 2. The extents of the LPC domains (orange boxes) used in the first-principles radar simulations (described in Section 3.2) and the global river database centerlines (described in Section 2.3) for (a) the Eastern United States; (b) a single scene in the Western United State, and (c) one particular LPC domain from the Eastern United States (c). For purposes of visualization, 1 km topography (units of meters above mean sea level) from GTOPO30 (USGS, 1996) is shown; note that GTOPO30 is not used for any analysis. Rivers with width greater than 250 m are plotted with heavy lines. Note that the colourbar for (a) and (c) are identical.

Cover Dataset (NLCD) (USGS, 2016) are used to specify the backscattering coefficient of land surfaces in the first principles radar simulations. SWOT processing requires a so-called "reference" water mask, in addition to the reference DEM described earlier. The reference mask is used to flag so-called "dark water" pixels (further described in Section 3.2). We use the global surface water inundation dataset of Pekel et al. (2016) as the reference mask.

3. Methods

3.1. Layover model formulation

Layover is a well understood phenomenon in radar imaging (see, for example, Curlander and McDonough, 1991), and its effects can be simulated directly given precise knowledge of the surface topography and the radar reflectivity. Existing global data sets of these surface properties are not sufficiently precise for direct, large-scale assessments of SWOT performance, however, as (in general) DEMs with resolution of approximately 1 m are required for accurate simulations, and such data are not available globally. We consequently develop a simplified model that gives a statistical description of layover-induced measurement errors for a scene rather than specific, high-fidelity realizations of errors within the scene. We refer to statistical expectation of measurement error as "uncertainty," characterized by its 68th percentile absolute error, in the remainder of the manuscript; this is consistent with how uncertainty is usually defined in the context of the SWOT mission (Esteban Fernandez, 2017). The theoretical derivation of the model is given in this section.

In order to give a statistical estimate of the layover-induced height error for a water body of interest, the model begins with the roughness of the topography as a statistical measure of the geometric variation in the surrounding land height that causes layover. Let the topographic roughness σ_z be defined as the standard deviation of the topographic height over a uniformly weighted 1 km $\times$1 km box centered on the

water body under consideration. The box size was chosen to be small enough to include the land topography closest to the river, but large enough to be effective for the range of river widths in the first-principles simulations. While some global rivers are wider than 1 km, we note that for these very large rivers, layover errors will be minimal, because layover-contaminated pixels will be a smaller fraction of the total number of pixels and because the layover contributions will be more random, as described below. We compute σ_z over both land and water pixels within each scene.

We choose the topographic roughness as a key model parameter because it can be readily evaluated from existing global DEMs, and it is robust to DEM resolution and accuracy, as confirmed by a comparison (not shown) between values of σ_z estimated from the lidar and SRTM DEMs described in Sections 2.1 and 2.2.

A single, statistical measure of the topographic roughness over a 1 km box is of course not sufficient to fully predict the specific effects of layover for a given realization of a scene geometry. In general, the errors for a given scene can be affected by topography that is farther than 1 km from the river and has larger height variations than described by σ_z. Therefore, define an effective topographic roughness $\tilde{\sigma}_z$ as

$$\tilde{\sigma}_z = C_T \sigma_z. \tag{1}$$

where C_T is a constant model parameter that scales the topographic roughness σ_z. This parameter also helps account for the fact that water in layover is generally at a lower elevation than the surrounding land, so the variability of the topography that contributes to layover is greater than the standard deviation of the elevations. (We assume that $C_T = 2$ globally based on the results of Section 4.2.) Note that C_T is the only model parameter whose value is derived empirically from direct simulations.

Layover is a geometric distortion that generally preserves along-track distances but projects coordinates in the cross-track direction. Therefore, for a river node P under observation, we define along-track and cross-track node widths as illustrated in Fig. 3. Assume that σ_z and $\tilde{\sigma}_z$ are evaluated at P, and define an effective river cross-track width w_y given by

$$w_y = \begin{cases} \left| \dfrac{w_a}{\sin \psi_r} \right| & \text{if } \left| \dfrac{w_a}{\sin \psi_r} \right| < w_{\max} \\ w_{\max} & \text{otherwise} \end{cases} \tag{2}$$

where w_a is the average river width (based on area in developing the model) over node P and ψ_r is the river flow direction at P relative to the cross-track direction for the viewing geometry of the observation. If the river is flowing purely in the cross-track direction, then ψ_r is 0 or 180°. The parameter $w_{\max}$ is a maximum cross-track width that prevents w_y from going to infinity when ψ_r goes to zero. This is not a realistic case, as the river banks would not be perfectly straight. We assume $w_{\max} = 10$ km.

Let the effective along-track or azimuth width w_x of the river be given by

$$w_x = \left| \frac{L_n w_a}{w_y} \right| \tag{3}$$

where L_n is the along-stream node length, such that the effective cross-track and along-track dimensions for layover modeling preserve the true node area. This approach preserves the number of independent radar samples, or looks, that observe the node, as the number of looks is an important parameter in determining the level of random measurement error.

The effective number N_x of along-track looks contributing to the node average is

$$N_x = \frac{w_x}{\delta_x} \tag{4}$$

where δ_x is the along-track resolution of the radar.

The effective number N_w of cross-track looks on the desired water surface is given by the effective width w_y divided by the ground-projected range resolution δ_y

$$N_w = \frac{w_y}{\delta_y}. \tag{5}$$

Given the incidence angle θ_{inc}, which represents the angle between the zenith at the node P and the vector pointing from P to the radar, the effective number N_c of layover-contaminated cross-track looks, which can be no larger than N_w, is given by

$$N_c = \begin{cases} \dfrac{\tilde{\sigma}_z}{\delta_y \tan \theta_{\text{inc}}} & \text{if} \dfrac{\tilde{\sigma}_z}{\delta_y \tan \theta_{\text{inc}}} < N_w \\ N_w & \text{otherwise} \end{cases} \tag{6}$$

where the factor of $\tan\theta_{\text{inc}}$ projects the vertical topographic variations into a horizontal water extent that is affected by layover, assuming planar wavefronts. This is illustrated in Fig. 1.

If a layover-flagging algorithm discards samples that are believed to be corrupted by layover, the number of remaining cross-track looks can be denoted as N_W, such that $0 \le N_W \le N_w$. Similarly, the number of remaining layover-contaminated samples can be denoted as N_C, such that $0 \le N_C \le N_c$. All results shown assume that no samples are flagged, so $N_W = N_w$ and $N_C = N_c$. See Section 5.3 for a discussion of layover flagging.

Let the water-to-land contrast R_{wl} be the ratio of the radar backscatter coefficients for water and land when each is considered individually, irrespective of layover. We assume that water is a factor of 10 brighter than land, consistent with Esteban Fernandez (2017), so $R_{wl} = 10$.

The resulting height estimate for node P is formed by averaging all node samples that contain water echoes, though some of the samples also contain undesired land echoes due to layover. Let R_{WL} be the effective ratio of desired water echo power to undesired land echo power due to layover after averaging:

$$R_{WL} = R_{wl} \frac{N_W}{N_C}. \tag{7}$$

Because the number of layover-contaminated samples cannot exceed the total number of water samples ($0 \le N_C \le N_W$), the effective water-to-land ratio in the measurement is no lower than the water-to-land contrast ($R_{WL} \ge R_{wl}$), although it can be much higher if there is little or no layover. When the land topography is random, the area of competing land that lays over into a given patch of a water surface can be very high for land surfaces that are sloped toward the radar at angles near θ_{inc}. However, nearby water patches that are affected by the opposing land slopes would likely be corrupted by correspondingly less land area as discussed in Section 5.2. The term R_{WL} describes the average contrast over the water body and over local variations in topography (recall that this model describes only statistical performance,

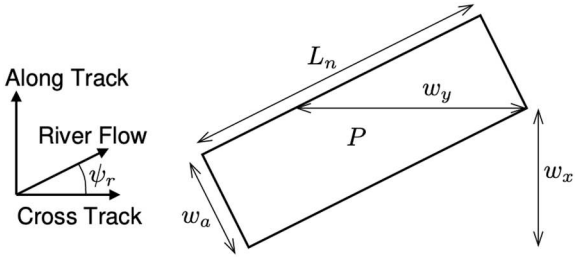

Fig. 3. Illustration of the assumed node geometry relative to the along-track and cross-track dimensions. In the figure, w_a is the river width, w_y represents the effective river cross-track width, L_n is the node spacing, w_x represents the effective river along-track width, and ψ_r is the river flow direction with respect to the cross-track direction.

not the effects for any given fine-scale realization of the geometry).

While the layover model assumes a static value of R_{WL}, the first-principles simulations do capture fine-scale variations in the land-water contrast as a function of land cover and topography. Successful calibration of the layover model (see below) demonstrates that the layover model is fairly robust to the assumption of static R_{WL}.

Note that this model considers only layover that maps land into water. It is also possible for layover to cause two different water features to contaminate each other, though this scenario is much less common.

Let R_{snr} be an effective signal-to-noise ratio (SNR) that accounts for thermal noise, geometric decorrelation, and other sources of random error, excluding layover. The SNR including layover could also be derived, but it is not needed in our formulation of the height bias due to layover. We use a heuristic model for R_{snr} to approximate the behavior of the random error curve vs. cross track position described in Esteban Fernandez (2017) rather than replicate the full SWOT performance calculations, as the complexity of the full calculation is unnecessary in this analysis.

The SNR in decibels is assumed to be

$$R_{snr}^{(\mathrm{dB})} = M_{0snr}\left[\cos\left(\frac{\pi(y - y_{0snr})}{2W_{0snr}}\right)\right]^2 + C_{0snr} \tag{8}$$

so the SNR as a linear ratio is

$$R_{snr} = 10^{(R_{snr}^{(\mathrm{dB})}/10)}. \tag{9}$$

Here, y is the cross-track distance of P from nadir, $M_{0snr} = 8.5$ dB, $y_{0snr} = 40$ km, $W_{0snr} = 40$ km, and $C_{0snr} = -2.5$ dB for the nominal case. This model gives a reasonable approximation of expected SWOT random-error performance in the absence of layover.

Finally, let the ambiguity height h_a be the height change that corresponds to one cycle (2π rad) of interferometric phase change. The ambiguity height varies with cross-track position and is given by

$$h_a = \frac{\lambda\rho}{B}\tan\theta_{\mathrm{look}}. \tag{10}$$

Here, λ is the radar wavelength, ρ is the slant range, B is the interferometric baseline length, and θ_{look} is the angle of the vector from the radar to the target with respect to nadir at the radar (note that θ_{look} is slightly less than θ_{inc} due to the variation in the local vertical direction with Earth curvature, which is significant for spaceborne InSAR observations). With the conventions of this model, h_a should always be positive. For SWOT, $\lambda = 8.3858$ mm, $\rho \approx 900$ km, and $B = 10$ m.

Now, following the derivations of the complex interferometric coherence γ that are well known in the context of volume scattering [see, for example, Eqs. (31, 62, 63) of Rosen et al., 2000 and the associated references therein], define the complex interferometric coherence γ_L due to layover and finite SNR as

$$\gamma_L = \frac{1 + \mathrm{sinc}(\tilde{\sigma}_z/h_a)\exp(j\pi\tilde{\sigma}_z/h_a)/R_{WL}}{1 + 1/R_{WL} + 1/R_{snr}} \tag{11}$$

where

$$\mathrm{sinc}(x) = \frac{\sin(\pi x)}{\pi x} \tag{12}$$

and

$$j = \sqrt{-1}. \tag{13}$$

Here, the scattering contribution from layover is assumed to be uniformly distributed statistically in height between 0 and $\tilde{\sigma}_z$ above the height of node P. This gives rise to the second additive term in the numerator of Eq. (11), since

$$\frac{1}{\tilde{\sigma}_z}\int_0^{\tilde{\sigma}_z}\exp\left(j\frac{2\pi}{h_a}z\right)\mathrm{d}z = \mathrm{sinc}(\tilde{\sigma}_z/h_a)\exp(j\pi\tilde{\sigma}_z/h_a). \tag{14}$$

The form of Eq. (14) is common in modeling signal penetration into scattering volumes such as vegetation in interferometric SAR contexts. It is applicable here even where signal penetration into the surface is not assumed, however, as the heights can still be distributed between 0 and over a node simply due to topographic variations across the horizontal extent of the node.

Note that actual penetration into the surface (as from vegetation) would tend to alter the model only to the extent that the penetration affects the topographic roughness of the scattering centers captured by $\tilde{\sigma}_z$. If the topographic roughness of the surface height dominates variation in the scattering centers due to penetration, penetration will have little additional impact.

A layover-induced bias h_L over the node arises from the nonzero phase of the coherence (the phase of γ_L is referenced to the true water height of the node):

$$h_L = \frac{h_a}{2\pi}\angle\gamma_L \tag{15}$$

where the phase $\angle\gamma_L$ is in radians.

Using the Cramer-Rao bound for the phase variance as described by Rosen et al. (2000), the phase standard deviation σ_ϕ, again in radians, is approximated by

$$\sigma_\phi = \sqrt{\frac{1}{2N_W N_x}\left(\frac{1 - |\gamma_L|^2}{|\gamma_L|^2}\right)} \tag{16}$$

so that the height standard deviation σ_h is given by

$$\sigma_h = \frac{h_a}{2\pi}\sigma_\phi. \tag{17}$$

Define the random height uncertainty E_{hnR} of a node as the expected error in the node-level height estimate, accounting for both node-scale bias and random variations in the estimated height over multiple, hypothetical realizations of the node with randomized wavelength-scale scattering variations. This uncertainty is taken to be

$$E_{hnR} = h_L + \sigma_h. \tag{18}$$

Here, we assume, for conservatism, a direct sum of the bias and random terms rather than a root sum of squares.

For a given observation, the bias term h_L is assumed to be a constant (in time) bias for the node, but a varying bias from node to node such that E_{hnR} can be treated nominally as a measure of the uncorrelated random error from node to node. The random term σ_h will generally be uncorrelated from node to node due to the randomness of speckle in the radar echoes. In reality, the bias term h_L may be somewhat correlated from node to node, but this effect will be relatively unimportant if the topography is rough compared to the ambiguity height such that the bias itself is small, if the node-to-node variation in roughness is big enough that the node-to-node correlation of the bias is low, and/or if the water-land contrast is high such that the overall impact of layover is small. Indeed, the small node-level biases from the first principles simulations shown in Section 4.2 suggest that this effect is indeed relatively small compared to the overall magnitude of reach-scale SWOT errors. A detailed investigation of the node-to-node correlation of height errors is outside the scope of this paper, however, as there are mechanisms other than layover for introducing such correlations. Below, we adopt a modification to the uncertainty expressions one would obtain for independent node height errors to approximately capture the effect of spatial correlation while still generally following the simplistic formulation that treats height errors as either uncorrelated from node to node or common over all nodes in a reach. This approach is consistent with the error framework of Esteban Fernandez (2017). A quantitative assessment of the sensitivity of the discharge results to node-to-node correlation is given in Section 4.5.

The height uncertainty over a reach is computed by first accounting for the reduction in random (but potentially spatially correlated) error from averaging multiple node height estimates, then applying an

estimate of the systematic errors that are assumed to be common over the reach.

Given a reach of length L_r, the number N_r of nodes of length L_n in the reach is given by $N_r = L_r/L_n$. The random height uncertainty E_{hrR} at the reach level is given by

$$E_{hrR} = \frac{\sqrt{\sum_k^{N_r} E_{hnRk}^2}}{N_r}\sqrt{\frac{L_c}{L_n}} \tag{19}$$

where E_{hnRk} is the height uncertainty E_{hnR} for node k, L_c is the effective length over which random errors are correlated due to layover or other effects, and the summation is over all nodes in the reach. We note that while we have treated the layover bias h_L as a random effect in Eq. (18) as described above, spatial correlation of both layover bias and other height errors may lead to correlation among the random part of the node-level height errors E_{hnR}. This is captured by L_c. For the quantitative results in Section 4.5, we take the nominal case for this study to be $L_c = L_n$, or uncorrelated random errors at the node scale. We also assess a conservative case with $L_c = 800$ m, which doubles the random part of the reach-scale height errors, since L_n is defined to be 200 m. Note that this doubling of random errors conservatively applies to random errors from all sources, not just random errors due to layover. We will consider both the nominal and conservative cases in the discharge analysis shown below.

The total height uncertainty E_{hrT} for the reach is then found by taking the root sum of the squares of the random uncertainty E_{hrR} over the reach and the systematic uncertainty E_{hS}:

$$E_{hrT} = \sqrt{E_{hrR}^2 + E_{hS}^2}. \tag{20}$$

Based on Esteban Fernandez (2017), we assume that $E_{hS} = 8.9577$ cm.

The slope uncertainty over a reach of length L_r is computed analytically from the model for the height uncertainty over each node, following the model of Section 6.3.2 of Esteban Fernandez (2017). The error-budget model assumes that the layover-induced height errors of the nodes are random and independent. In order to approximate the effects of node-to-node correlation on the random height errors, let the model slope random uncertainty E_{srR} be given for an effective node height random error $\widetilde{E}_{hnR}$ (defined below) by

$$E_{srR} = \widetilde{E}_{hnR}\sqrt{\frac{12}{N_r L_r^2}}\sqrt{\frac{L_c}{L_n}}, \tag{21}$$

where the $\sqrt{L_c/L_n}$ term scales the reach-level slope error just as it scaled the reach-level height error in Eq. (19) by the effective number of nodes over which the node-scale random height errors are correlated.

The node random height uncertainty $\widetilde{E}_{hnR}$ here assumes that the node errors are identically distributed. This, of course, may not strictly be the case. Eventually, if the distributions of random height errors for individual nodes are known, the slope estimator could weight the node heights according to the uncertainty on each node (this complexity is not captured above). For now, however, we keep the assumption of identically distributed node height errors over a reach, and, consequently, uniform weights in the slope estimator. There are several reasons for this assumption. First, the assumption simplifies the slope uncertainty model and facilitates a more intuitive understanding of the results and the associated sensitivities. Second, the assumption allows the model to mirror the analysis of the SWOT error budget (Esteban Fernandez, 2017). Third, the assumption provides a useful bounding case for the slope uncertainty.

Given the above discussion, define the effective node random height uncertainty $\widetilde{E}_{hnR}$ as the root mean square over the reach of the individual node height uncertainties from the model as

$$\widetilde{E}_{hnR} = \sqrt{\frac{1}{N_r}\sum_k^{N_r} E_{hnRk}^2}. \tag{22}$$

The total slope uncertainty E_{srT} for the reach, including both random slope uncertainty E_{srR} and systematic slope uncertainty E_{sS}, is then given by

$$E_{srT} = \sqrt{E_{srR}^2 + E_{sS}^2}. \tag{23}$$

We assume that $E_{sS} = 3.3599 \times 10^{-6}$ rad based on the SWOT error budget (Esteban Fernandez, 2017).

3.2. Layover model calibration

In order to calibrate and to validate the model for layover-induced height and slope errors described in Section 3.1, we compare model-predicted errors to the errors obtained from direct, first-principles simulations. The simulator software is the same as that used for some of the analyses in Esteban Fernandez (2017), as well as that used, for example, by Frasson et al. (2017), Domeneghetti et al. (2018), Grippa et al. (2019), and Langhorst et al. (2019).

Lidar DEMs were generated from the LPC data by keeping the first lidar returns where available, thereby simulating the effects of vegetation canopy-top scattering to the extent possible, as penetration of the Ka-band SWOT radar signals into vegetation is expected to be minimal (Bamler and Hartl, 1998). The DEMs were also processed to fill voids in water areas and to smooth artifacts that would give physically unrealistic height variations over water surfaces. The smoothing algorithm involves image segmentation, histogram filtering, and moving-average filtering to allow different water features to be smoothed separately, thereby avoiding unrealistic artifacts when nearby water features are at different elevations. Note that the smoothing operation results in water heights that might differ somewhat from the true water heights. In fact, in some cases, the water surface might even be higher than the surrounding land. However, this occurs only in areas with significant topographic variations such that the water height errors of the DEMs would not be expected to affect the conclusions of this analysis. Note that while layover is often visualized with land that is higher and farther from nadir than water, the effect is geometrically symmetric such that errors would also arise for water that is higher than land. Indeed, the DEMs for this analysis need only be generally representative of realistic water features. It is not important for the DEMs to match reality exactly. The water mask for the simulations were constructed from a combination of the National Hydrography Dataset, the SRTM Water Body Dataset, and the River Database, as described in Section 2.4.

The simulations assumed realistic water reflectivities, including a model for specular ("dark") water and representative land reflectivities based on NLCD land cover types. The Ka-band brightness as a function of incidence angle for each non-water NLCD type is modeled as a look-up table that was derived from Global Precipitation Mission data over NLCD classes (Esteban Fernandez, 2017). The water scattering brightness is modeled as a function of wind speed and incidence angle using a custom geophysical model function (GMF) derived from a combination of geometric optics and AirSWOT data. The wind speed for each scene was randomly generated using a k^{-2} spatial wavenumber spectrum with a mean wind speed value over the whole scene derived from calendar year 2005 National Centers for Environmental Prediction - National Center for Atmospheric Research Reanalysis version 1 numerical weather prediction simulations.

In evaluating the model, σ_z was computed from the near-global (between -60° and 60° latitude) SRTM DEM version 4 (Jarvis et al., 2008) as the sample standard deviation of elevations within a 1×1 km square kernel. The water-land contrast R_{wl} for evaluating the model was assumed to be 10 dB (not the actual, spatially varying contrast used in the direct simulations).

The height measurements from the direct simulation were aggregated into node-height estimates with the RiverObs software (Rodriguez et al., 2014). The node length L_n was assumed to be 200 m

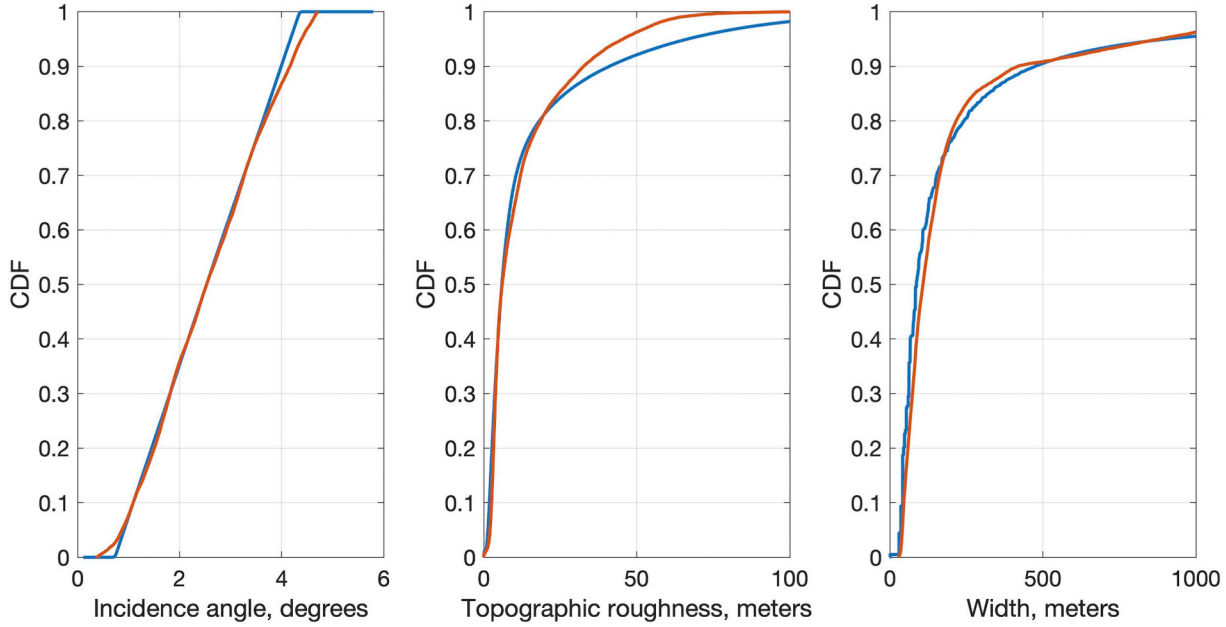

Fig. 4. Characteristics of the nodes used in the model calibration and validation (red) and in the global river database (blue): (left) distribution of incidence angle θ_{inc}; (center) distribution of topographic roughness σ_z, limited to 100 m; (right) distribution of river width w_a, limited to 1000 m. (For interpretation of the references to colour in this figure legend, the reader is referred to the web version of this article.)

both when processing the direct simulations and evaluating the model. However, the model captures the physical mechanisms relating the height error to the node length (primarily the number of looks), so the model is applicable to other node lengths as well. Reach-level quantities from the direct simulation were not assessed, as the spatial distribution of the nodes across scenes in the data set does not give enough reaches for a useful statistical characterization, and the analytical propagation of errors from the node level to the reach level is straightforward in any event.

Nodes are defined according to the River Database described in Section 2.3. In total, 21,414 unique nodes are covered by the set of simulations. From the nominal SWOT orbit, these nodes are observed from different viewing directions (from ascending or descending orbit passes and to the left or to the right of nadir) across the simulations, giving 39,714 unique combinations of viewing geometry and geographic location. The total number of node observations considered, including overlapping coverage, is 41,233, over 148 simulated scenes. Note that nodes with overlapping geometric coverage still have different realizations of water reflectivity, random surface fluctuations (speckle), and instrument noise, so they still contribute to the statistical characterization of height error.

Cumulative distribution functions (CDFs) of the incidence angle θ_{inc}, the topographic roughness σ_z, and the river width w_a over these nodes is illustrated in Fig. 4. The nodes are well distributed over the useful range of SWOT incidence angles (about 0.7–4.3°) and over river widths from approximately 20–1000 m. Fig. 4b shows that the global distribution of σ_z is well-represented by the first-principles simulations, up to the 85th percentile. Although the first-principles simulations somewhat underrepresent high values of σ_z, our results shown below indicate that the worst layover effects are actually for low values of σ_z.

The node height errors between the direct simulation and the uncertainty from the model were compared as follows. The nodes were binned on the predicted node-level height uncertainty from the model. For each bin, statistics of the realizations of the height error from the direct simulation were computed over all nodes within the bin. The statistics from the direct simulation for each bin were then compared to the bin-center predicted uncertainty from the model.

An example image from one of the direct simulations is shown in Fig. 5a. This image overlays the radar image power (indicated by the grayscale brightness) and the wrapped phase of the interferogram (indicated by the colour) after an initial stage of along-track averaging to reduce noise. The image is represented in slant-plane radar coordinates, with range increasing toward the right. Consequently, topographic features over land "lay over" toward the left. The image corresponds to a small segment of a larger simulated scene covering the Smoky Hill River in Kansas. The center of the radar image is located at 38.957° latitude and −96.913° longitude and covers approximately 6.6 km along-track and 5.2 km cross-track extent as projected onto the ground. Because the image is in radar coordinates, it is flipped (and slightly rotated) with respect to natural ground coordinates such that north is approximately toward the top of the image, but west is approximately toward the right. For comparison, a shaded-relief image from the lidar DEM that was used as the input to the simulation is shown in Fig. 5b. The shaded-relief image is represented in ground coordinates (not radar coordinates), but it is shown flipped here such that west is to the right in order to align it more closely with the radar image in Fig. 5a.

Some features of the simulated radar example of Fig. 5a are notable in the context of layover. First, the water pixels are considerably more reflective than the land pixels, which are near the noise floor, so land echoes that lay over into water areas will have relatively little influence on water measurements. Second, even with the lack of rugged terrain in this area, layover is still evident in the darker land areas; layover of land into other land in the lower half of the image makes the topographic relief appear "fallen over" toward the left. However, the wrapped interferogram phase of land areas is distributed between 0 and 2π radians because of the small ambiguity height h_a. Layover contamination of water will therefore be more of a random error than a bias. Third, while nearly all of the river is in fact in layover geometrically (this may not be evident visually but can be confirmed in the data), there is no easily discernible impact of layover on the phase of water pixels. Note that the variation in phase over the river near the upper right corner of the image (where the colour changes from magenta to lavender) is not due to layover; it is associated with errors in the reference surface used to flatten the phase.

3.3. Layover model global application

In order to apply the layover model globally, σ_z was computed from

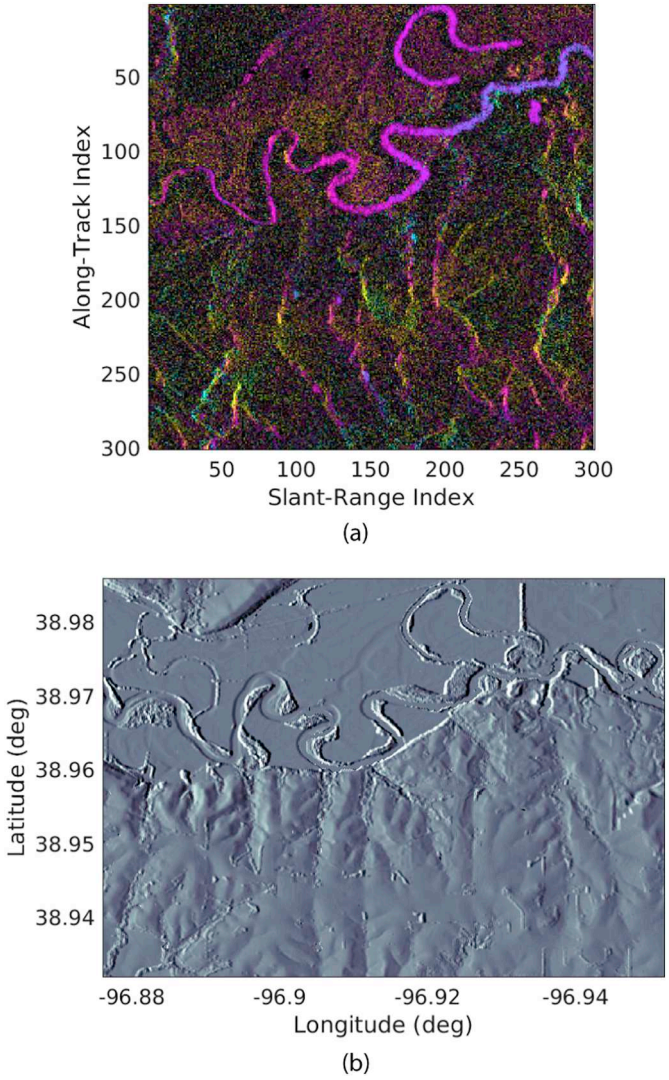

Fig. 5. Example simulated radar data (a) and the associated shaded-relief image from the DEM (b). The simulated radar data are shown in the slant-plane coordinates of the radar image, with range increasing toward the right and imaging time or along-track coordinate increasing downward. The image brightness depicts the radar image power, which is related to the surface reflectivity, while the color represents the wrapped interferogram phase. The shaded-relief image is flipped such that east is to the left in order to more closely align it with the radar coordinates. (For interpretation of the references to color in this figure legend, the reader is referred to the web version of this article.)

the SRTM DEM of all points falling inside a 1 km by 1 km window. We associated the topographic roughness (σ_z) with river nodes in the river database by searching for the closest σ_z to a river node. Subsequently, we identified passes observing each node by computing the shortest distance between the node and the SWOT passes. Nodes located farther than 10 km and closer than 60 km to the pass groundtrack are assumed to be observed by that pass. Finally, we computed the relative heading of the river at each node with respect to passes observing that node.

Reaches and nodes that fall within lakes were excluded from analysis, as were all rivers narrower than 100 m. River reaches shorter than 9.5 km were also excluded from analysis, in order to focus on the impact of layover, rather than reach length; see Frasson et al. (2017) for an example of how reach length impacts height uncertainty for SWOT. After these exclusions, a total of 6,843,139 nodes and 220,924 reaches were analyzed. As this study focuses on reach-averaged discharge, which is not computed at the node scale, we focus on reaches in subsequent analysis. Fig. 6 shows a map of river slopes, which illustrates the global extent of the analysis.

3.4. Discharge uncertainty model

During SWOT mission operations, river discharge will be computed using simple flow laws (Durand et al., 2016). In this study, we assume use of a modified version of Manning's equation:

$$Q = \frac{1}{n}(A_0 + \delta A)^{5/3} W^{-2/3} S^{1/2} \tag{24}$$

where Q is the river discharge, n is the coefficient describing the force of friction resisting river flow, A_0 is the unobserved part of the river cross-sectional area, δA is the temporal anomaly in cross-sectional area, W is river width, and S is river slope. Here δA, W and S are SWOT observables, and n and A_0 are flow law parameters computed using so-called mass-conserved flow law inversion algorithms (Gleason et al., 2017). For the purposes of this paper, we can assume $\delta A \approx W\delta H$, where H is the water surface elevation. In this study, we will assess the "direct" effect of layover-controlled increase in uncertainty in river height and slope on river discharge by applying first-order error propagation to Eq. (24). Future work will consider effects of layover on discharge inversions via the discharge parameters.

In order to compute the effect of SWOT observation uncertainty on river discharge uncertainty, we follow the approach of Yoon et al. (2016). We consider the effect of layover only on river height and slope, as the effect on river width accuracy is expected to be minimal. Ignoring uncertainty in flow law parameters, and in river width, the river discharge relative uncertainty is:

$$\left(\frac{\sigma_Q}{Q}\right)^2 = \left(\frac{5}{3}\frac{\sigma_{\delta A}}{A_0 + \delta A}\right)^2 + \left(\frac{1}{2}\frac{\sigma_S}{S}\right)^2 \tag{25}$$

where the standard deviation of each term is denoted by σ. Under the assumptions noted above, $\sigma_{\delta A}$ is given by:

$$\sigma_{\delta A} \approx W\sigma_H\sqrt{2}. \tag{26}$$

We approximate the total river cross-sectional area (i.e. $A_0 + \delta A$) as the product of river width and depth. We estimate depth by combining downstream hydraulic geometry relationships for width and depth, viz. Eqs. 15 and 16 of Moody and Troutman (2002). This yields a prediction of depth as a function of width. Substituting this and Eq. (26) into Eq. (25) gives:

$$\left(\frac{\sigma_Q}{Q}\right)^2 = \left(\frac{5}{3}\frac{\sigma_H\sqrt{2}}{c\left[\frac{W}{a}\right]^{f/b}}\right)^2 + \left(\frac{1}{2}\frac{\sigma_S}{S}\right)^2 \tag{27}$$

where the downstream hydraulic geometry exponents and coefficients a, b, c, and f are taken from Moody and Troutman (2002). Eq. (27) expresses relative discharge uncertainty in terms of uncertainty in height and slope, along with river width and slope, and downstream hydraulic geometry coefficients. Essentially, this is similar to work presented by Biancamaria et al. (2010), but with the independent variable being the river width, which is measured to high accuracy by Allen and Pavelsky (2018), with slope included explicitly, and links to the detailed height and slope uncertainty models presented above.

4. Results

4.1. Example layover output

In order to illustrate how layover varies with cross-track distance and topographic standard deviation, we first consider an example river with the layover model of Section 3.1. Fig. 7 shows example output from the layover model, using a value of $C_T = 2.0$, as described in the following section, for a 100 m wide river, with 200 m node spacing, flowing perpendicular to the SWOT groundtrack (i.e. the relative

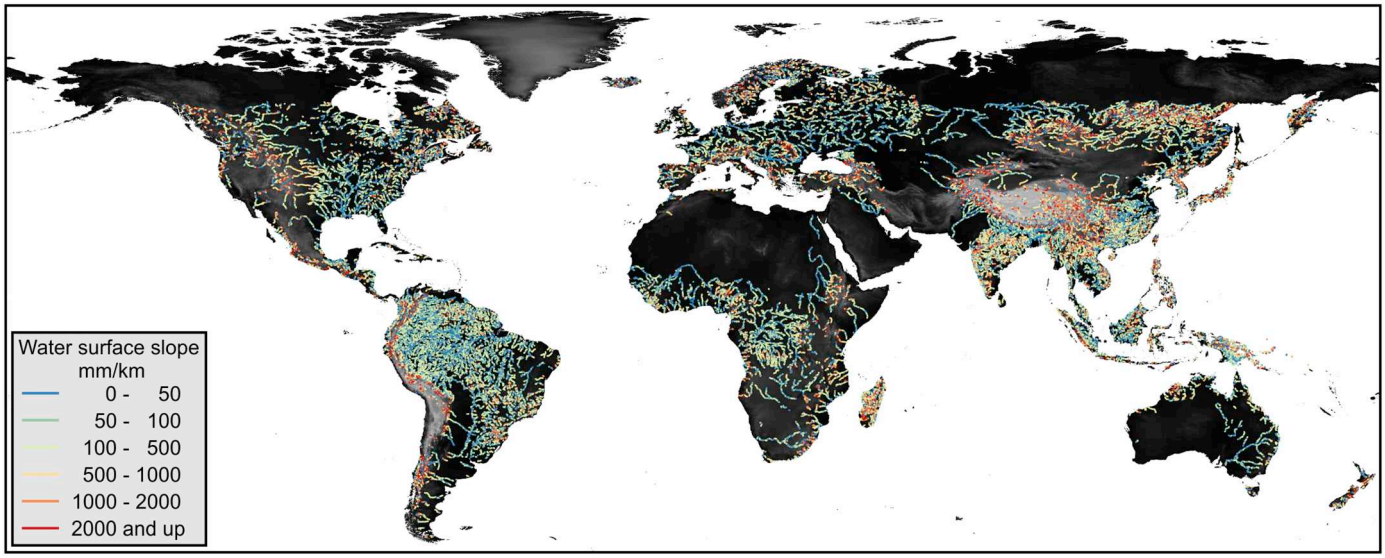

Fig. 6. Water surface slopes computed from SRTM as described in Frasson et al. (2019) used for the evaluation of discharge uncertainty.

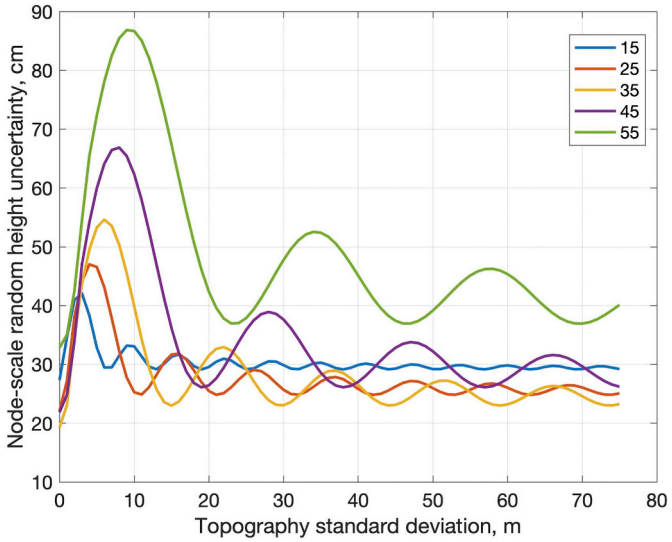

Fig. 7. Node-scale random uncertainties as a function of topographic standard deviation at different cross-track distances (in kilometers) calculated with Eq. (18).

heading ψ_r is $\pi/2$). Our results show that layover-induced error is highest for rivers with relatively low topographic roughness measured at high incidence angles. Layover-induced uncertainty in SWOT observations reach a maximum at relatively low values of σ_z, and vary widely across the swath. Random uncertainties reach maxima between 2 and 8 m of σ_z, with larger maxima in the far swath. The peak value ranges from 40 cm in the near swath to ~85 cm in the far swath.

4.2. Model calibration

Fig. 8 shows a comparison of the layover-induced node height uncertainty predicted by the model of Section 3.1 and the statistics of the errors computed through direct simulation following the methodology of Section 3.2. Note that the bins on the horizontal axis of Fig. 8 are not uniformly spaced. They are defined such that each bin contains approximately 400 nodes, giving 103 bins total.

The median error from the simulations (red curve) is relatively close to zero, confirming that layover does not introduce a significant overall height bias. This also suggests that the node-to-node correlation of the layover-induced biases, which would usually be positive, is not a dominant source of error.

The dark blue curve represents the 68th percentile of the absolute value of the height error (over the nodes in each model bin) from the simulations. This quantity is most directly comparable to the uncertainty that is computed by the model. This quantity is shown rather than the standard deviation or the RMS error because it is less sensitive to outliers in the simulated data. This curve follows the 1:1 line reasonably well, although the model conservatively overpredicts the errors somewhat for errors greater than approximately 0.3 m. The correlation coefficient is 0.912. The agreement indicates that the model of Section 3.1 usefully predicts the expected errors from layover.

Together, the curves for the 10th, 25th, 50th, 75th, and 90th percentiles in Fig. 8 show the distributions of the errors from the direct simulation for each bin of the theoretical model in a manner similar to that of a box plot. A traditional box plot is difficult to interpret given the number and spacing of the bins on the horizontal axis, however. The bin spacing was chosen so that the point density provides an indication of the distribution of the data over the height uncertainty from the theoretical model (i.e., over the horizontal axis). The global CDF of the model-predicted uncertainty is also shown in Fig. 9.

4.3. Layover impacts on height

Fig. 10 shows example height uncertainty estimates at reach scale in the vicinity of the upper Missouri River from the model of Section 3.1. Height uncertainty decreases with increasing river width and thus the lowest values of height uncertainty fall along the mainstem Missouri, Yellowstone and South Saskatchewan rivers.

Fig. 11 shows a CDF of the global distribution of reach-scale height uncertainty with and without layover included. The height uncertainty distribution is highly skewed, with most values falling near approximately 10 cm, and a long tail. Globally, swath position has the largest control on these low percentage outliers. The worst 1% of uncertainty values occur for reaches near swath edges. The effect of layover is to cause height errors to increase minimally: the 68th percentile increases from 9.4 to 10.4 cm. This does cause a significant change in the total number of reaches that fall below 10 cm, however, which is the nominal science requirement. The fraction of reaches with height error <10 cm decreases from 95 pct to 60 pct due to layover. The conservative analysis, doubling the random height error component as described in Section 3.1, is also shown in Fig. 11. The 68th percentile further increases to 13.9 cm. However, these modest increases in actual height

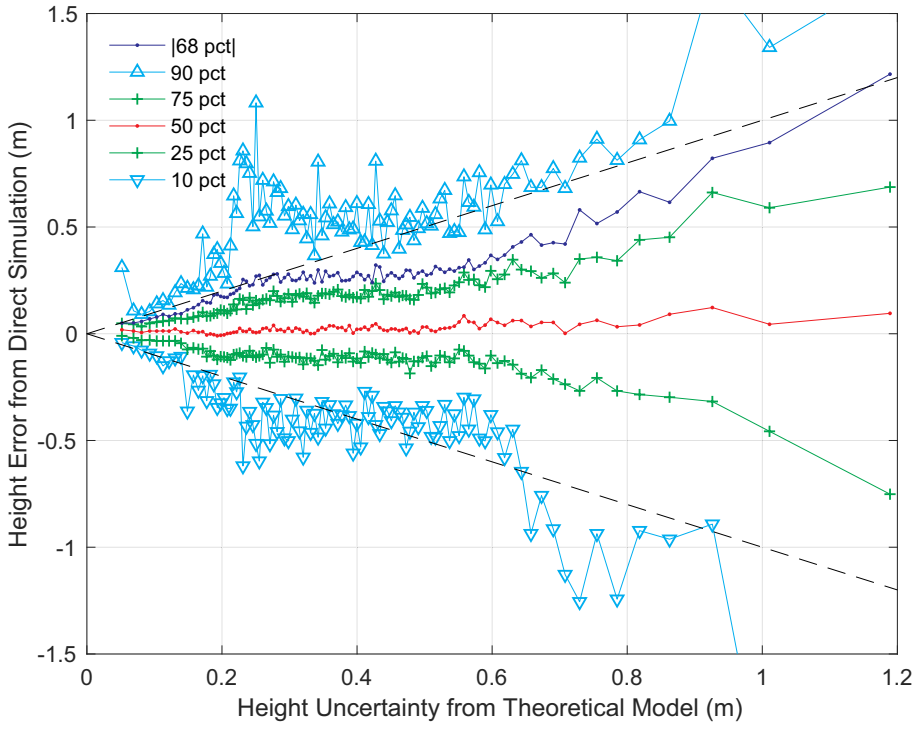

Fig. 8. Statistics of layover-induced height error on nodes from direct simulation over bins of predicted layover-induced height uncertainty from the simplified theoretical model of Section 3.1. The dark blue curve represents the 68th percentile of the absolute height error from the direct simulation. From bottom to top, the other coloured curves represent the 10th, 25th, 50th, 75th, and 90th percentiles of the simulated errors, thereby characterizing the statistics of the errors from the direct simulation for each bin on the horizontal axis in a manner similar to what might be represented in a box plot. The dashed black lines represent 1:1 lines for visual reference. If the theoretical model were a perfect statistical representation of the direct simulation, the dark blue curve would follow the 1:1 line exactly. (For interpretation of the references to colour in this figure legend, the reader is referred to the web version of this article.)

uncertainty are simply not enough of a change to substantially impact the science that can be accomplished with SWOT observations; we illustrate this point below by propagating this uncertainty to river discharge.

4.4. Layover impacts on slope

Fig. 12 shows example slope uncertainty estimates for the same region shown in Fig. 10. Generally, the slope uncertainty spatial pattern

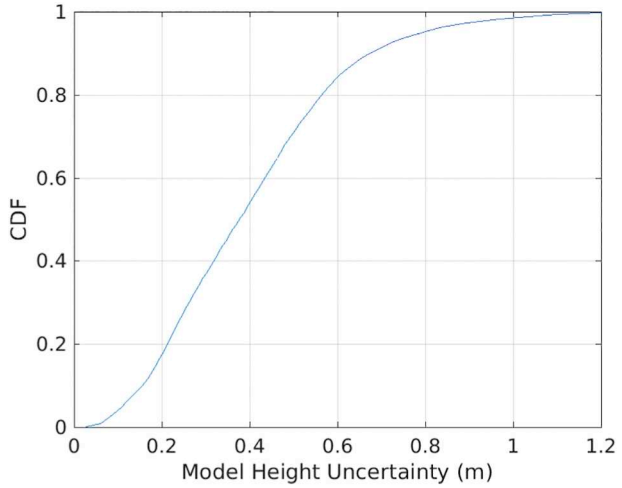

Fig. 9. Distribution of the model-predicted height uncertainty over the nodes considered in the analysis.

mirrors that of the height uncertainty. Note however that the number of occurrences of reaches with double the nominal uncertainty (34 mm/km slope or 20 cm height) is far greater for slope, as indicated by the greater prevalence of reaches shaded red in Fig. 12 compared with Fig. 10. The conservative case, doubling random height errors as described in Section 3.1, causes a further increase in the 68th percentile of error to 35 mm/km. The reason that reach-scale slope error increases more than height error due to doubling the node-scale random height error is simply that total slope errors are more dominated by random error, whereas total reach-scale height errors are more dominated by systematic error. As noted in Section 3.1, systematic height error is approximately 9 cm, whereas systematic slope error is approximately 3×10^{-6} rad. Comparison of the systematic values with the CDFs in Figs. 11 and 13 shows that systematic height errors are much larger compared to the total.

Fig. 13 shows a global histogram of slope uncertainty estimates with and without layover effects included. Slope errors increase moderately: the 68th percentile increases from 1 cm/km to 1.7 cm/km due to layover. This is a significant change: only 10% of global reaches have slope errors $>$ 1.7 cm/km in the no-layover case. Fig. 14 shows that slope uncertainty increases somewhat as a function of river width. The widest rivers (~1000 m) are not significantly affected by layover, but for the narrower rivers (~100 m), both the median slope uncertainty and the interquartile range are significantly larger in the case where layover errors are included.

4.5. Layover impacts on discharge

Fig. 15 shows estimates of river discharge uncertainty for global reaches with and without layover, showing the impact of layover on

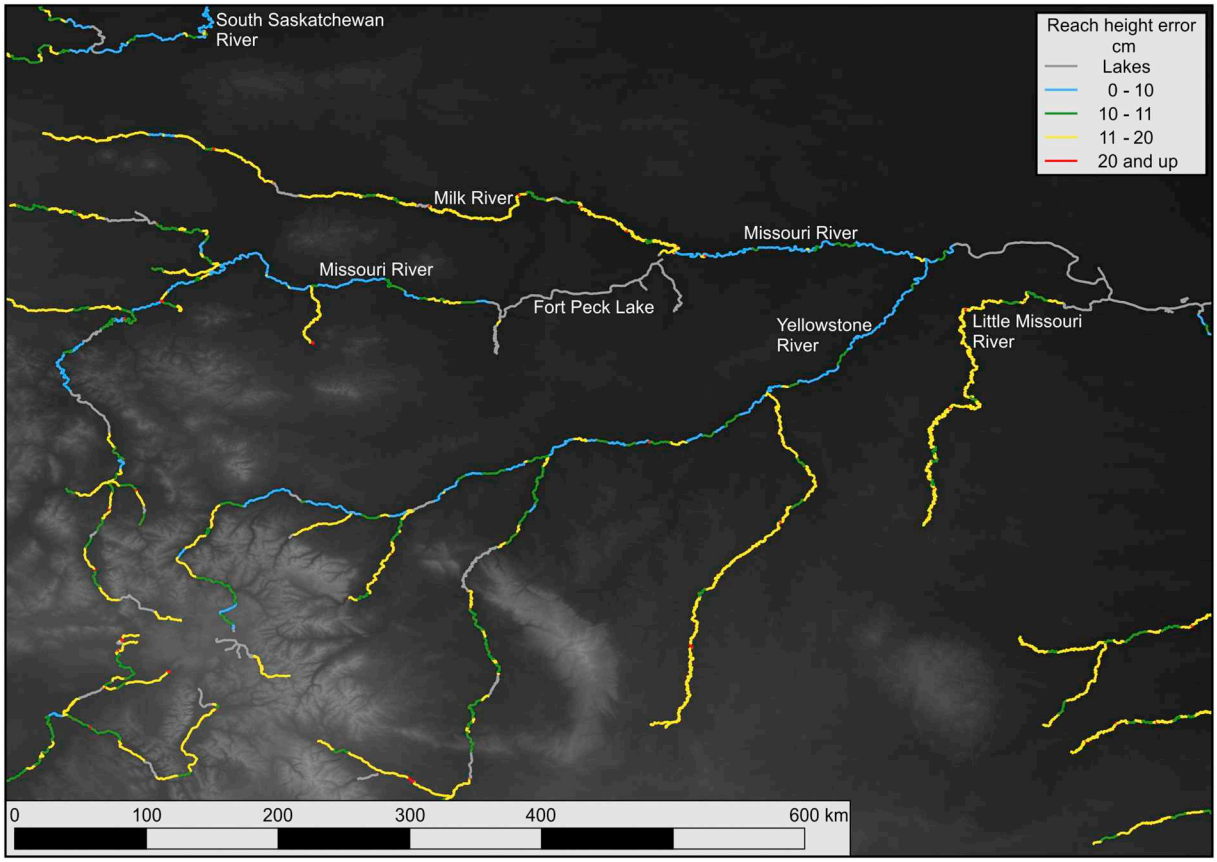

Fig. 10. Example reach-scale height errors in the upper Missouri River basin are shown. Each reach shows the mean observation error across all passes.

height and slope presented in the previous two sub-sections. To understand the sensitivity of these results to the various assumptions made throughout, we also present the global discharge uncertainty for a conservative-case analysis where we have doubled the random height and consequent slope uncertainty due to all sources including layover, referred to as the "double random error" case.

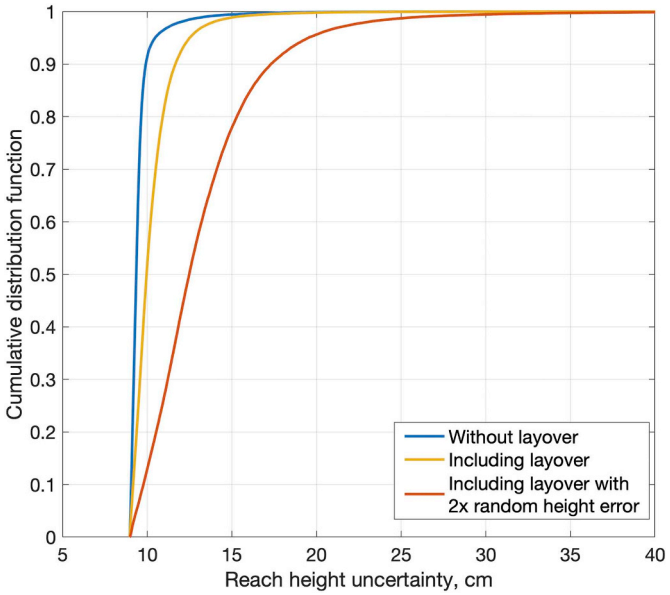

Fig. 11. Layover impacts on global height errors at reach scale. The yellow and red lines indicate the "nominal" and "conservative" layover cases, respectively, as described in Section 3.1. (For interpretation of the references to colour in this figure legend, the reader is referred to the web version of this article.)

Generally, layover causes discharge errors to increase minimally: the 68th percentile increases from 12% to 13% for the expected level of error due to layover. However, layover increases the number of reaches for which slope errors will be too high to use Manning's equation (nominally taken as a discharge uncertainty of 0.2). In the "no layover" case, 12% of global reaches will have slope errors too large to use Manning's equation. When layover is included, Manning's equation will be inapplicable for 17% of reaches. These findings have implications for methods used in SWOT river discharge products: height and width alone will be used to estimate discharge for reaches where Manning's equation is inapplicable. Note that methods to compute discharge directly from satellite measurements of river height and width have been used for decades (e.g. Kouraev et al. (2004), Gleason et al. (2014), Pavelsky (2014)), and will be adapted for use with SWOT measurements. Doubling the random height error results in further degradation: the 68th percentile of discharge uncertainty increases to approximately 20%, underscoring the need to develop methods for estimating discharge that do not use SWOT slope measurements: such methods will be critical if layover causes height and slope errors to be closer to the "double random error" case.

5. Discussion

5.1. *The Grand Canyon illustration*

The relatively minor impact of layover on SWOT measurements may be surprising to readers who are accustomed to topography measurements of land derived from interferometric SAR (Bamler and Hartl, 1998). The schematic illustration in Fig. 16 may help give an intuitive explanation for why layover does not pose a greater problem for SWOT. In this cartoon, an imaged water feature lies at the bottom of a deep

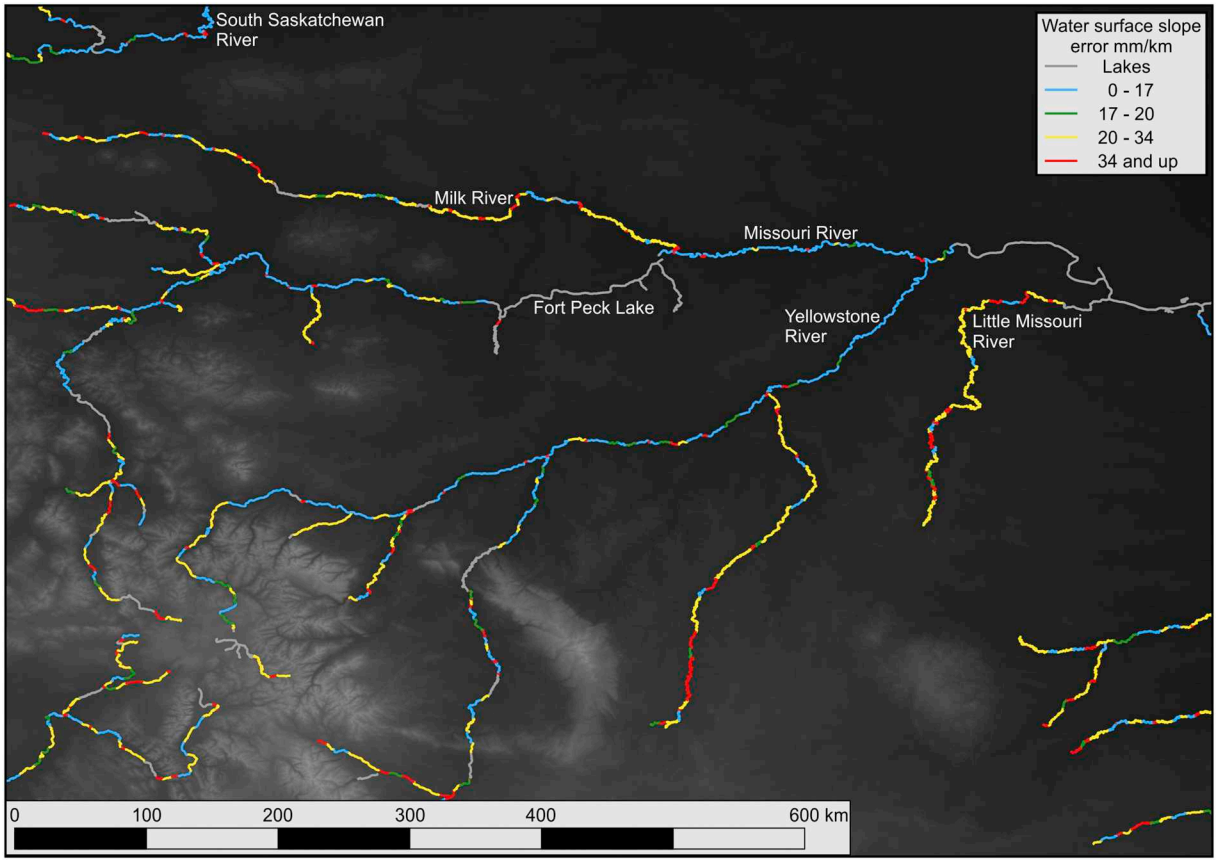

Fig. 12. Example reach-scale slope errors in the upper Missouri River basin are shown. Each reach shows the mean observation error across all passes.

canyon with steep sides, as might be the case for the Colorado River through the Grand Canyon. The diagonal black lines indicate contours of constant slant range from the radar; parcels of land at the same slant range as the water lay over into the water and give undesired radar echoes that compete with the desired water echoes. Note, however, that most of the land in the scene lays over into other land. Such layover of land into other land is of no consequence for the primary SWOT measurements of water. Moreover, observe that if the canyon were deeper, the competing land echoes due to layover would come from different locations (farther in cross track, or further to the right for the upper parcel of competing land in the figure), but the area of the competing land would not increase. At this geometric bound, in which the water feature is fully covered in area by layover, the impact of the contamination is still bounded (on average) by the relative contrast between the reflectivities of water and land. At SWOT incidence angles, water is much more reflective than land, so the layover echoes from land are relatively weak. Therefore, while the steep incidence angles of the SWOT measurement give rise to the prevalence of layover in the first place, they also imply scattering characteristics which make layover less of a problem.

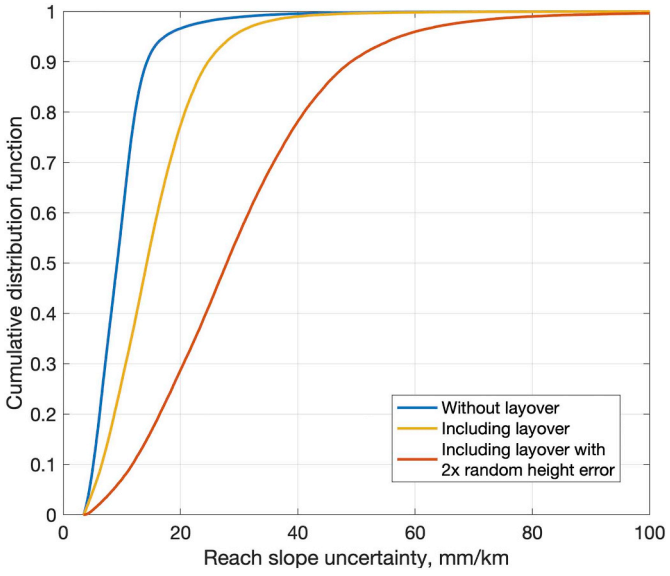

Fig. 13. Layover impacts on global slope uncertainty. The yellow and red lines indicate the "nominal" and "conservative" layover cases, respectively, as described in Section 3.1: doubling the random part of the height error causes the slope error to increase. (For interpretation of the references to colour in this figure legend, the reader is referred to the web version of this article.)

In fact, for the SWOT viewing geometry, very little surface relief is required to make the cartoon shown in Fig. 16 applicable. With an incidence angle of 2° near the middle of the SWOT swath, as little as 4 m of surface height variation (including vegetation) near a water body that is 100 m wide could cause the entire water body to be in layover geometrically. The minor impact of layover on SWOT is thus not because layover can be avoided geometrically but because the contaminating echoes due to layover are significantly weaker than the desired water echoes.

The layover echoes are also likely to be quite random in phase due to the small SWOT ambiguity heights (10–60 m over the swath), although this is not represented in the cartoon illustration of Fig. 16. In fact, if the land contaminating the water were actually as flat as illustrated, it would cause a bias rather than a random error. Such a bias is the mechanism for the peak in layover-induced error at low topographic roughness in Fig. 7. Random errors, on the other hand, decrease with spatial averaging. Therefore, perhaps counter-intuitively, rivers in

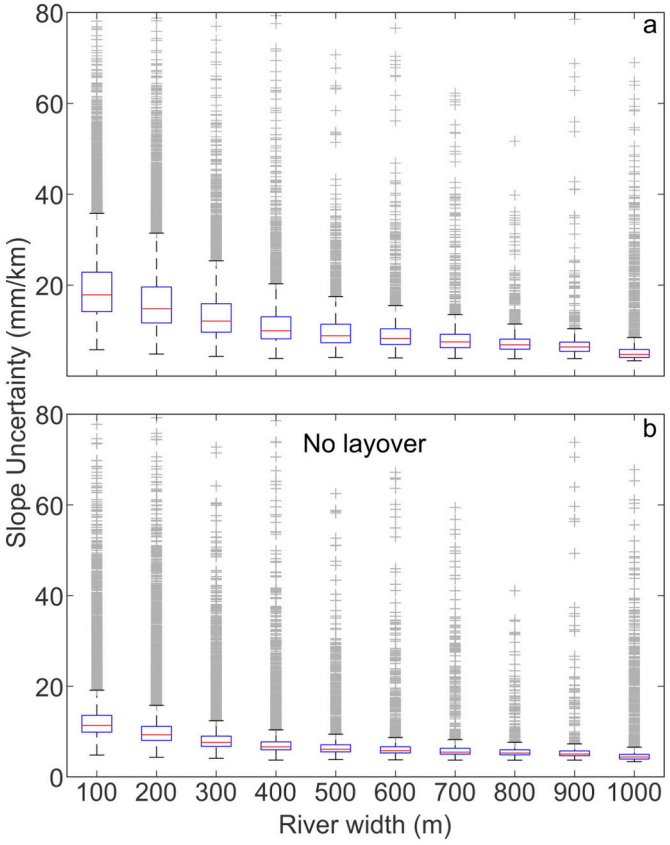

Fig. 14. Layover impact on slope errors categorized by river width.

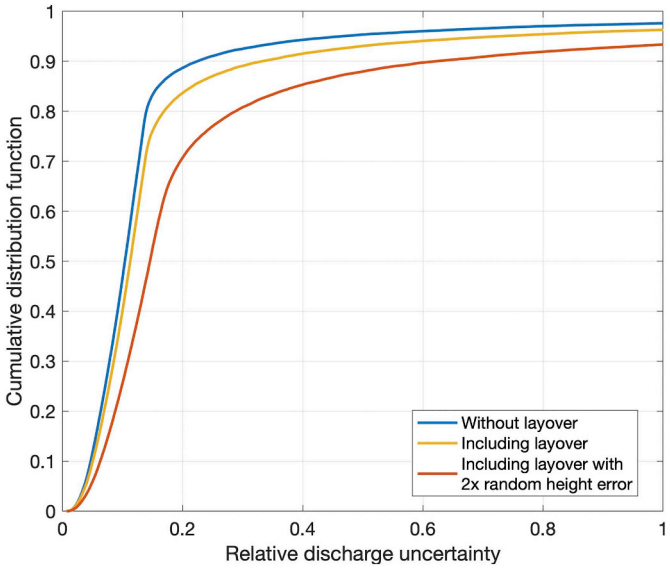

Fig. 15. CDFs of global discharge errors due to height and slope errors only. The blue curve shows the effect of height and slope errors propagated through the Manning's equation without layover effects. The yellow and red lines indicate the "nominal" and "conservative" layover cases, respectively, as described in Section 3.1. Note that doubling the random part of the height error causes the slope error to increase as well; increases in both height and slope uncertainty are propagated to discharge via Eq. (27). (For interpretation of the references to colour in this figure legend, the reader is referred to the web version of this article.)

relatively flat areas may exhibit the largest height errors due to layover.

5.2. Spatially varying vs. flat topography

While flat topography, as illustrated beyond the canyon walls in Fig. 16, affects the water in a spatially homogeneous manner, spatially varying topography affects the water surface inhomogeneously. Namely, where the land surface is sloped toward the radar at angles near θ_{inc}, a large area of the land will map into a small area of the water and could contaminate the measurement for that parcel of the water surface quite significantly. However, where the land surface is sloped away from the radar, a lesser area of land (relative to a flat surface) maps into a given area of water. This is illustrated conceptually in Fig. 17. The echo power from Land Surface 2 is considerably higher than the echo power from Land Surface 1 where the slope of Land Surface 2 is unfavorable (in the nearest slant-range cell to the radar for this example). However, this water area is limited in extent, and the echo power from Land Surface 2 is commensurately lower than for Land Surface 1 for the other slant-range cells that intersect the backslope. To first order, the total land contamination is similar between the different cases once averaged over the water surface. A detailed discussion of the actual land echo power, which also depends on the surface reflectivity, is beyond the scope of this discussion, although it is captured by the first-principles simulation used to validate the analytical model. Here, it suffices to note qualitatively that the effects of spatially varying topography are described statistically by the model even when extended parts of the land surface have slopes near θ_{inc}.

5.3. Does flagging lessen the impact of layover?

An intuitive approach for attempting to mitigate errors due to layover might be to identify and flag water samples that are in layover and to exclude them when averaging to compute the node height. We investigated this flagging strategy, and while a lengthy discussion of this topic extends beyond the scope of this paper, we give a brief summary of the work here because the conclusion was somewhat surprising and because it provides additional insights on the discussion above: flagging layover pixels and discarding them in fact increases rather than decreases the overall error. This finding was borne out both in the direct simulations and in a generalized version of the simple model that accounts for the number of flagged samples in N_C and N_W in Eq. (7). We found this to be true even under ideal conditions when layover samples could be perfectly identified.

This effect can be explained qualitatively as follows. Water samples in layover contain the sum of the complex interferometric signals from both water and land. Therefore, while these layover samples contain undesired, corrupting land echoes, they also contain useful information

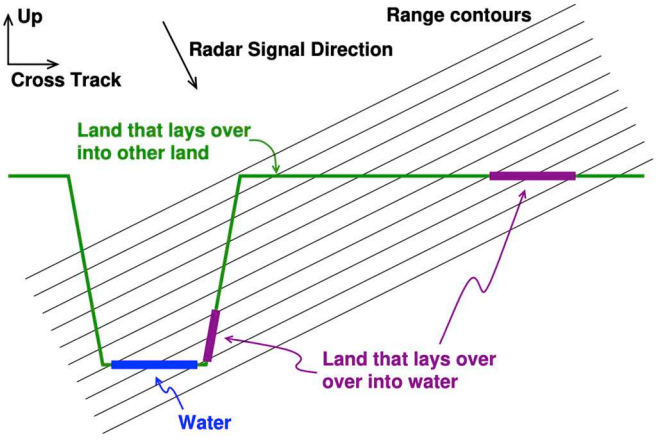

Fig. 16. Illustration of layover for a case such as the Grand Canyon.

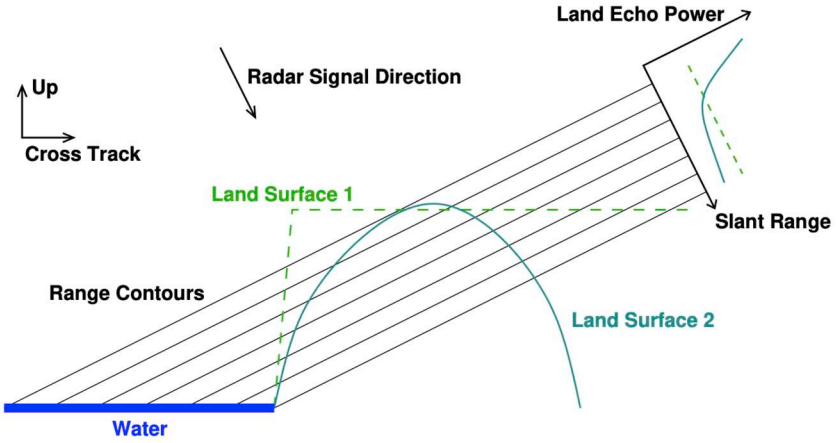

Fig. 17. Illustration of layover for alternative land cases of flat land (dashed curve labeled "Land Surface 1") and sloped land (solid curve labeled "Land Surface 2") with an associated conceptual plot of the echo power only from land as a function of slant range for each case at the upper right. The echo power from land is proportional to the land area in each range-resolution cell (represented here by the distance along the land surface between the range contours).

about the water height. In fact, given the generally high water-land contrast (R_{wl}), the land signal tends to be considerably weaker than the desired water signal. The land signal is also not significantly stronger than the instrument noise floor. Moreover, the land signal, when averaged at node scales, tends to appear random due to the phase wrapping that occurs when the topographic roughness is greater than the ambiguity height ($\bar{\sigma}_z > h_a$). Therefore, as the undesired signal due to layover behaves effectively like a random noise source that is not much stronger than the background instrument noise, it is better to include the layover samples during averaging because it is better to have more noisy samples than fewer noisy samples to average.

Framed in terms of the analytic model of Section 3.1, discarding flagged samples reduces the number of contaminated samples N_C only at the expense of also reducing the total number of water samples N_W. Even in an ideal case where N_C goes to zero and R_{WL} goes to infinity, the interferometric correlation γ_L is still limited by the finite SNR, as indicated by Eq. (11). The phase variance then increases as N_W decreases in Eq. (16).

In short, flagging and discarding layover samples generally hurts more than it helps because the errors due to layover tend to be random and comparatively small in the first place, so the samples in layover are better used for beating down the random variations from both layover and noise.

6. Conclusion

Although layover contamination is expected to be ubiquitous in SWOT measurements of river height and slope, it will not completely obscure river measurements. Instead, the effect of layover will be to increase uncertainty in measurements, for affected reaches. Our analysis shows that layover will only increase expected reach-scale height errors by a marginal amount: the 68th percentile of reach errors is expected to increase from 9.4 to 10.4 cm. The impact on the 68th percentile of slope uncertainty will likely be greater, from 10 mm/km to 17 mm/km. When these errors are propagated to river discharge, we find that layover will not significantly impact discharge for most reaches: the 68th percentile uncertainty increases from 12% to 13%. Instead, the larger impacts from layover affect the tails of the slope and discharge uncertainty distributions. Thus, layover leads to a significant increase in the number of reaches where slope uncertainty is large compared to the average reach slope: (17% up from 12%). Thus, this study has important implications in determining how to best compute river discharge from SWOT measurements for low-slope reaches.

Another outcome of this investigation is the conclusion that layover mitigation strategies that simply flag and exclude data tend to hurt more than help the resulting height errors. Future investigations of layover mitigation may involve estimating a layover impact quantity that can be used to optimally aggregate to river nodes and reaches (e.g., appropriately weight laid-over pixels) to minimize the resulting uncertainty.

We have focused the discussion in this paper on the ways in which layover is expected to impact river discharge. Thus, our height error model captures the impact of layover by assuming that node-scale layover biases increase the reach-scale slope error and random height error. As a result, we did not compute or present expected height biases due to layover at the reach scale. Indeed, in areas impacted by layover, layover-induced height biases at the reach scale may persist, especially in relatively flat areas. Frasson et al. (2017) examine this effect in context of a first-principles radar simulation. Future work should further characterize the impact of layover on reach-scale height bias errors for the SWOT mission.

Finally, additional effort will be needed to more thoroughly characterize SWOT phenomenology in general, both an important research objective in itself and in order to help validate or refine the assumptions used in this layover analysis. These include assumptions on the surface scattering, the statistics of topographic variations, node-to-node correlation, and error contributions from sources other than layover.

Declaration of Competing Interest

The authors declare that they have no known competing financial interests or personal relationships that could have appeared to influence the work reported in this paper.

Acknowledgement

We would like to acknowledge the financial support received through the SWOT Algorithm Definition Team (ADT) contract to the Ohio State University (subcontract #1613807) and the University of North Carolina (subcontract #1616855). A portion of this work was performed at the Jet Propulsion Laboratory, California Institute of Technology, under contract with NASA. Government sponsorship acknowledged.

References

USGS, 2016. NLCD 2011 land cover (2011 edition, amended 2014) - national geospatial data asset (NGDA) land use land cover. https://doi.org/10.5066/P937PN4Z.

Frasson, R.P.D.M., Wei, R., Durand, M., Minear, J.T., Domeneghetti, A., Schumann, G., Williams, B.A., Rodriguez, E., Picamilh, C., Lion, C., Pavelsky, T., Garambois, P.,

2017. Automated river reach definition strategies: applications for the surface water and ocean topography mission. Water Resour. Res. 53, 8164–8186. https://doi.org/10.1002/2017wr020887.
Frasson, R.P.D.M., Pavelsky, T.M., Fonstad, M.A., Durand, M.T., Allen, G.H., Schumann, G., Lion, C., Beighley, R.E., Yang, X., 2019. Global relationships between river width, slope, catchment area, meander wavelength, sinuosity, and discharge. Geophys. Res. Lett. 46, 3252–3262. https://doi.org/10.1029/2019gl082027.
Allen, G.H., Pavelsky, T.M., 2018. Global extent of rivers and streams. Science 361. https://doi.org/10.1126/science.aat0636.
Bamler, R., Hartl, P., 1998. Synthetic aperture radar interferometry. Inverse Problems 14, R1–R54. https://doi.org/10.1088/0266-5611/14/4/001.
Biancamaria, S., Andreadis, K.M., Durand, M., Clark, E.A., Rodriguez, E., Mognard, N.M., Alsdorf, D.E., Lettenmaier, D.P., Oudin, Y., 2010. Preliminary characterization of SWOT hydrology error budget and global capabilities. IEEE J. Sel. Top. Appl. Earth Observ. Remote Sensing 3, 6–19. https://doi.org/10.1109/jstars.2009.2034614.
Biancamaria, S., Lettenmaier, D.P., Pavelsky, T.M., 2016. The SWOT mission and its capabilities for land hydrology. Surv. Geophys. 37, 307–337. https://doi.org/10.1007/s10712-015-9346-y.
Curlander, J., McDonough, R., 1991. Synthetic Aperture Radar: Systems and Signal Processing. Wiley, pp. 384 Chapter 8.2.
Domeneghetti, A., Schumann, G.J.P., Frasson, R.P.D.M., Wei, R., Pavelsky, T.M., Castellarin, A., Brath, A., Durand, M.T., 2018. Characterizing water surface elevation under different flow conditions for the upcoming swot mission. J. Hydrol. 561, 848–861.
Durand, M., Gleason, C.J., Garambois, P.A., Bjerklie, D., Smith, L.C., Roux, H., Rodriguez, E., Bates, P.D., Pavelsky, T.M., Monnier, J., Chen, X., Baldassarre, G.D., Fiset, J., Flipo, N., Frasson, R.P.D.M., Fulton, J., Goutal, N., Hossain, F., Humphries, E., Minear, J.T., Mukolwe, M.M., Neal, J.C., Ricci, S., Sanders, B.F., Schumann, G., Schubert, J.E., Vilmin, L., 2016. An intercomparison of remote sensing river discharge estimation algorithms from measurements of river height, width, and slope. Water Resour. Res. 52, 4527–4549. https://doi.org/10.1002/2015wr018434.
Esteban Fernandez, D., 2017. SWOT Mission Performance and Error Budget. Technical Report. NASA Jet Propulsion Laboratory.
Farr, T.G., Rosen, P.A., Caro, E., Crippen, R., Duren, R., Hensley, S., Kobrick, M., Paller, M., Rodrguez, E., Roth, L., Seal, D., Shaffer, S., Shimada, J., Umland, J., Werner, M., Oskin, M., Burbank, D., Alsdorf, D., 2007. The shuttle radar topography mission. Rev. Geophys. 45. https://doi.org/10.1029/2005rg000183.
Fjørtoft, R., Gaudin, J.-M., Lalaurie, J.C., Mallet, A., 2014. KaRIn on SWOT: characteristics of near-nadir Ka-band interferometric SAR imagery. IEEE Trans. Geosci. Remote Sens. 52, 2172–2185.
Gleason, C.J., Smith, L.C., Lee, J., 2014. Retrieval of river discharge solely from satellite imagery and atmanystations hydraulic geometry: sensitivity to river form and optimization parameters. Water Resour. Res. 50, 9604–9619. https://doi.org/10.1002/2014wr016109.
Gleason, C.J., Durand, M.T., Garambois, P.A., 2017. Tracking river flows from space. Eos 98. https://doi.org/10.1029/2017EO078085.
Grippa, M., Rouzies, C., Biancamaria, S., Blumstein, D., Cretaux, J.F., Gal, L., Robert, E., Gosset, M., Kergoat, L., 2019. Potential of SWOT for monitoring water volumes in Sahelian ponds and lakes. IEEE J. Sel. Top. Appl. Earth Observ. Remote Sensing 12, 2541–2549. https://doi.org/10.1109/jstars.2019.2901434.
Jarvis, A., Reuter, H., Nelson, A., Guevara, E., 2008. Hole-Filled SRTM for the Globe Version 4. URL: http://srtm.csi.cgiar.org.
Kouraev, A.V., Zakharova, E.A., Samain, O., Mognard, N.M., Cazenave, A., 2004. Ob' river discharge from TOPEX/Poseidon satellite altimetry (1992–2002). Remote Sens. Environ. 93, 238–245. https://doi.org/10.1016/j.rse.2004.07.007.
Langhorst, T., Pavelsky, T.M., Frasson, R.P.D.M., Wei, R., Domeneghetti, A., Altenau, E.H., Durand, M.T., Minear, T., Wegmann, K.W., Fuller, M.R., 2019. Anticipated improvements to river surface elevation profiles from the surface water and ocean topography mission. Front. Earth Sci. 07. https://doi.org/10.3389/feart.2019.00102.
Moody, J.A., Troutman, B.M., 2002. Characterization of the spatial variability of channel morphology. Earth Surf. Process. Landf. 27, 1251–1266. https://doi.org/10.1002/esp.403.
NASA JPL, 2013a. NASA Shuttle Radar Topography Mission Water Body Data V003. URL: https://lpdaac.usgs.gov/products/srtmswbdv003/.
NASA JPL, 2013b. NASA Shuttle Radar Topography Mission Global 1 Arc Second. https://doi.org/10.5067/MEaSUREs/SRTM/SRTMGL1.003.
Pavelsky, T.M., 2014. Using width–based rating curves from spatially discontinuous satellite imagery to monitor river discharge. Hydrol. Process. 28, 3035–3040. https://doi.org/10.1002/hyp.10157.
Pavelsky, T.M., Durand, M.T., Andreadis, K.M., Beighley, R.E., Paiva, R.C., Allen, G.H., Miller, Z.F., 2014. Assessing the potential global extent of SWOT river discharge observations. J. Hydrol. 519, 1516–1525. https://doi.org/10.1016/j.jhydrol.2014.08.044.
Pekel, J.F., Cottam, A., Gorelick, N., Belward, A.S., 2016. High-resolution mapping of global surface water and its long-term changes. Nature 540, 418–422. https://doi.org/10.1038/nature20584.
Rees, W.G., 2001. Physical Principles of Remote Sensing, 2nd edn. Cambridge University Press, pp. 320–344 chapter 9.6 Synthetic Aperture Radar.
Rodriguez, E., Fore, A., Williams, B., 2014. RiverObs. https://github.com/SWOTAlgorithms/RiverObs.
Rosen, P.A., Hensley, S., Joughin, I.R., Li, F.K., Madsen, S.N., Rodriguez, E., Goldstein, R.M., 2000. Synthetic aperture radar interferometry. Proc. IEEE 88 (333), 382. https://doi.org/10.1109/5.838084.
USGS, 1996. Global 30 arc-second elevation (GTOPO30). URL. https://doi.org/10.5066/F7DF6PQS.
USGS, 2017. Lidar Point Cloud - USGS National Map 3DEP Downloadable Data Collection. URL: https://www.sciencebase.gov/catalog/item/4f70ab64e4b058caae3f8def.
USGS, 2019. National Hydrography Dataset. URL: https://www.usgs.gov/core-science-systems/ngp/national-hydrography/national-hydrography-dataset.
Yoon, Y., Garambois, P.A., Paiva, R.C.D., Durand, M., Roux, H., Beighley, E., 2016. Improved error estimates of a discharge algorithm for remotely sensed river measurements: test cases on Sacramento and Garonne Rivers. Water Resour. Res. 52 (278), 294. https://doi.org/10.1002/2015wr017319.